

# Supplementary information

## Table of Contents

Section S1: Synthesis and materials screening .....	2
S1.1 Synthesis of pre-screening and reference samples .....	2
S1.2 Pre screening .....	3
Section S2: Characterization of Cu-Sb-S phases .....	3
S2.1 SEM before reduction .....	3
S2.2 EDX mapping before reduction.....	3
S2.3 XPS peaks before reduction .....	4
Section S3: Electrochemical performance of Cu-Sb-S phases .....	4
S3.1 XRD of reference samples.....	4
S3.2 Stability test .....	5
S3.3 Benchmarking against other works .....	5
S3.4 ECSA .....	6
Section S4: Post-reduction characterization and remnant sulfur.....	6
S4.1 CV.....	6
S4.2 ICP of electrolyte.....	7
S4.3 EDX mapping after reduction.....	7
S4.4 XPS peaks after reduction .....	8
S4.5 SAED after reduction .....	8
S4.6 SEM after reduction.....	8
S4.7 TEM after reduction.....	9
S4.8 Phase diagram .....	10
S4.9 Rietveld refinement of SK sample after reduction .....	11
Section S5: DFT calculations .....	12
S5.1 Atomic structures of sulfur-decorated Cu <sub>2</sub> Sb(100) systems .....	12
S5.2 Sulfur Stability Analysis.....	13
S5.3 Additional Computational Details on the Computational Hydrogen Electrode Approach .....	15
S5.4 Adsorption metrics analysis.....	16
S5.5 2e <sup>-</sup> CO <sub>2</sub> RR and HER catalytic activity analysis .....	19
S5.6 Other DFT data.....	20
References .....	23

## Section S1: Synthesis and materials screening

### S1.1 Synthesis of pre-screening and reference samples

- For colloidal nanoparticle synthesis:
  - For  $\text{Cu}_{1.8}\text{S}$ , 7.5 mmol of copper(II) acetylacetonate, 3 mL of 1-dodecanethiol and 3 mL of oleylamine were dissolved in 24 mL of 1-octadecene in a 250 mL three-neck flask and the mixture degassed under flowing nitrogen for 30 min at 150°C. The mixture was then heated to 250°C for 1 h under nitrogen atmosphere for the formation of nanoparticles.
  - For  $\text{Sb}_2\text{S}_3$ , 2.75mmol of antimony(III) acetate, 3 mL of 1-dodecanethiol and 3 mL of oleylamine were dissolved in 24 mL of 1-octadecene in a 250 mL three-neck flask and the mixture degassed under flowing nitrogen for 30 min at 150°C. The mixture was then heated to 250°C for 5 min under nitrogen atmosphere for the formation of nanoparticles.
  - For  $\text{Cu}_2\text{SnS}_3$ , 2.5mmol of copper(II) acetylacetonate, 1.25mmol of tin(IV) acetylacetonate, 3 mL of 1-dodecanethiol and 3 mL of oleylamine were dissolved in 24 mL of 1-octadecene in a 250 mL three-neck flask and the mixture degassed under flowing nitrogen for 30 min at 150°C. The mixture was then heated to 250°C for 1 h under nitrogen atmosphere for the formation of nanoparticles.
- For solvothermal synthesis of  $\text{CuInS}_2$ , 0.4mmol of copper(II) chloride dihydrate, 0.4mmol of indium(III) chloride and 0.9mmol of thiourea were dissolved in 50ml of ethylene glycol. The mixture was then transferred to a 120ml PTFE-lined steel autoclave, placed in an oven and heated at 180°C for 24h.
- For  $\text{Cu}_4\text{Sb}$  alloy electrodeposited on carbon paper, 10 mg of carbon black and 100  $\mu\text{l}$  of Nafion ionomer solution (5%) was dispersed in 2 mL of ethanol and sprayed with an airbrush gun onto a 6 cm by 6 cm CeTech (CT) GDL280 carbon paper. Then, 7 mmol of copper(II) chloride dihydrate, 1.75 mmol of antimony(III) chloride and 28 mmol of trisodium citrate dihydrate were dissolved in 70 mL of water. The carbon paper was then connected to a single-compartment 3-electrode cell and  $-1.4\text{ V}$  vs.  $\text{Ag}/\text{AgCl}$  electrode was applied for 120 s to electrodeposit Cu-Sb alloy.
- For desulfurized tetrahedrite (DS TH) sample, the TH sample synthesized and deposited on carbon paper beforehand as described under the methods section was reduced under  $-2\text{A}$  (including the back side of the carbon paper, so for catalyst is approximately  $-1\text{A}/\text{cm}^2$ ) for 10 min in 1M  $\text{KHCO}_3$ .

## S1.2 Pre screening

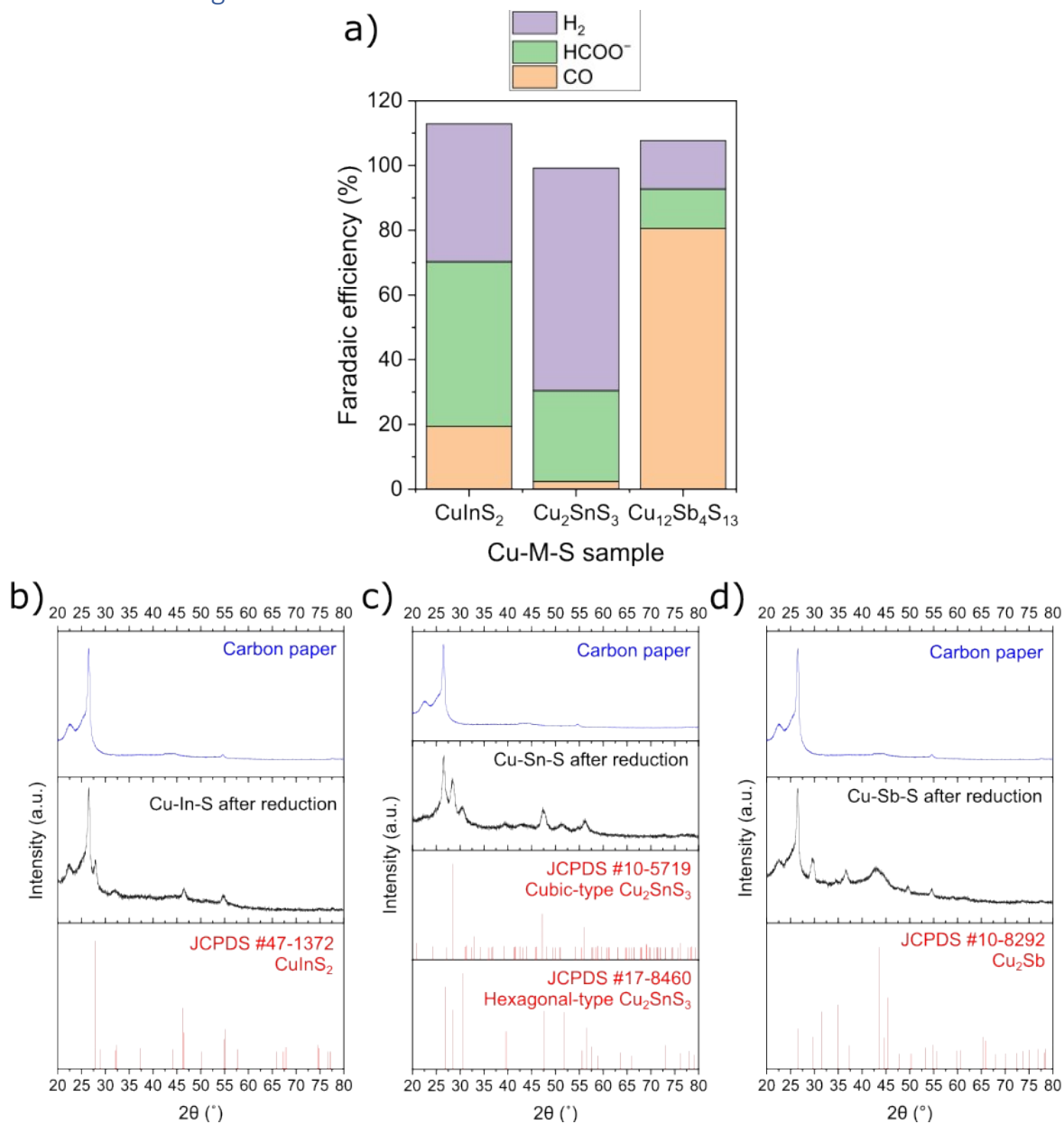


**Figure S1:** a) Faradaic efficiency at -1V vs RHE and b-d) XRDs after reduction of Cu-In-S, Cu-Sn-S and Cu-Sb-S samples. The reference peaks for Cu-In-S are of cubic CuInS<sub>2</sub>, the reference peaks for Cu-Sn-S are of cubic and hexagonal Cu<sub>2</sub>SnS<sub>3</sub>, while the reference peaks for Cu-Sb-S are of Cu<sub>2</sub>Sb

## Section S2: Characterization of Cu-Sb-S phases

### S2.1 SEM before reduction

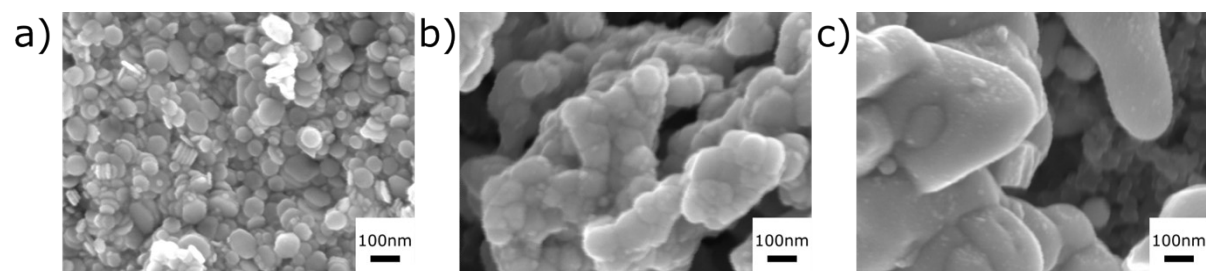


**Figure S2:** Close up SEM images of the three catalyst samples on carbon paper before reduction. a) SK b) TH c) CS

### S2.2 EDX mapping before reduction

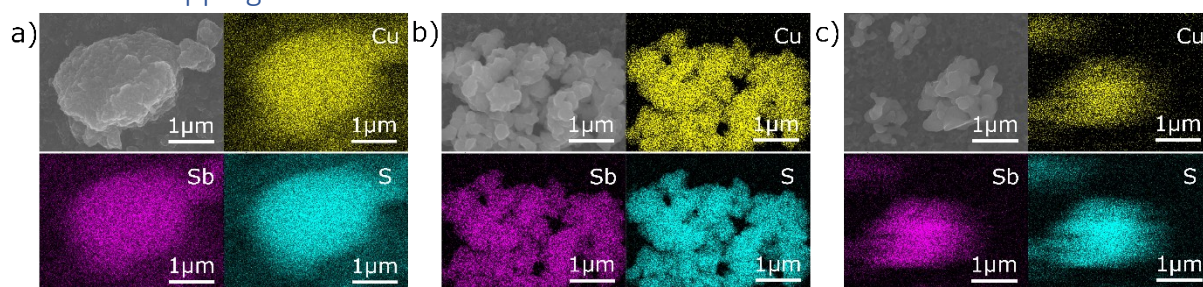


**Figure S3:** EDX mapping of the three catalyst samples on carbon paper before reduction. a) SK b) TH c) CS

### S2.3 XPS peaks before reduction

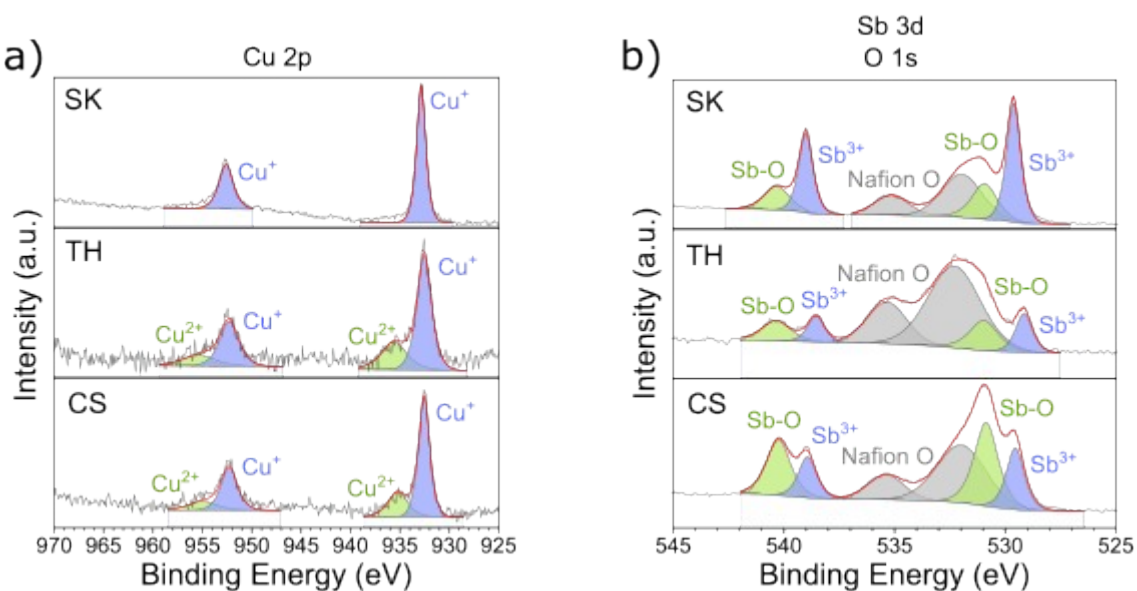


**Figure S4:** XPS peaks of the three catalyst samples on carbon paper before reduction. a) Cu 2p peaks b) Sb 3d and O 1s peaks

## Section S3: Electrochemical performance of Cu-Sb-S phases

### S3.1 XRD of reference samples

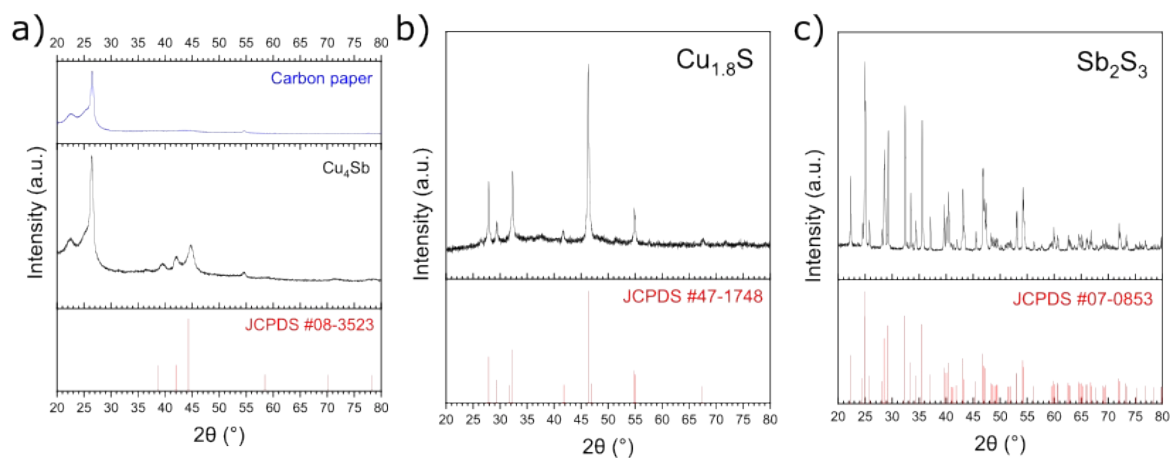


**Figure S5:** XRD peaks of reference samples. Electrodeposited a) Cu<sub>4</sub>Sb and powder b) Cu<sub>1.8</sub>S c) Sb<sub>2</sub>S<sub>3</sub>

### S3.2 High current density test

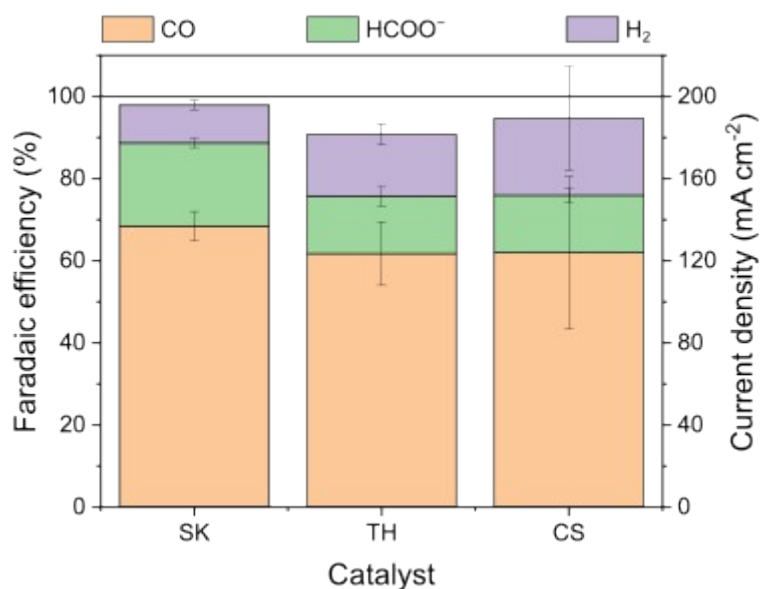


**Figure S6:** Electrochemical CO<sub>2</sub> reduction of the three samples in applied constant 200 mA cm<sup>-2</sup> current density. To accommodate the high current density, carbon black at half of the weight of the catalyst was added to the catalyst inks in the middle of sonication prior to spraying on carbon paper.

### S3.3 Stability test

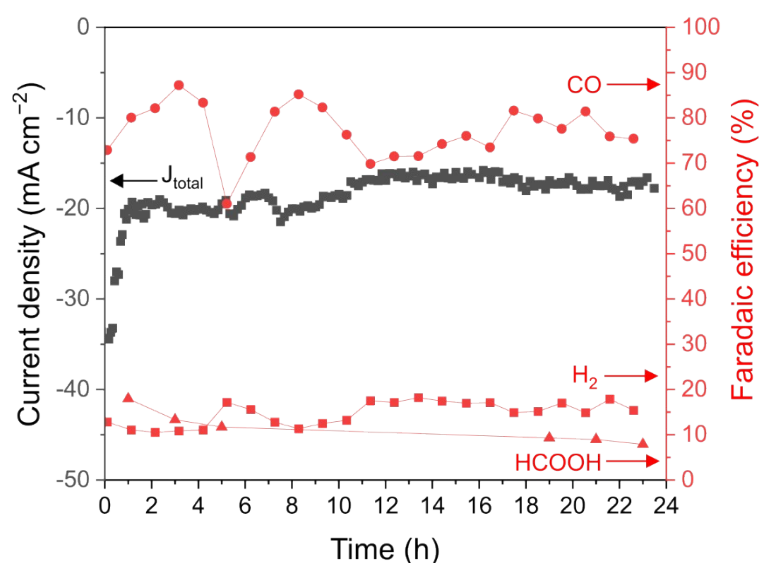


**Figure S7:** Stability test of TH sample done for 24 hours at -1V vs RHE.

### S3.4 Benchmarking against other works

**Table S1:** Benchmarking against other similar catalysts in literature

Catalyst	Electrolyte	Potential (V vs. RHE)	CO partial current density (mA/cm <sup>2</sup> )	CO <sub>2</sub> RR main product	Reference
<b>Cu-Sb catalysts</b>					
<b>CuO-Sb<sub>2</sub>O<sub>3</sub>/CB Nanocomposites (Cu:Sb of 10:1)</b>	0.1 M KHCO <sub>3</sub>	-0.8	4.5	CO	[1]
<b>Sb-modified Cu (galvanic displaced)</b>	0.1 M KHCO <sub>3</sub>	-1.1	4.5	CO	[2]
<b>Cu<sub>2</sub>Sb decorated Cu nanowire arrays</b>	0.1 M KHCO <sub>3</sub>	-0.9	6	CO	[3]
<b>Sb-doped Cu/Cu<sub>2</sub>O catalyst</b>	0.1 M KHCO <sub>3</sub>	-0.9	6.3	CO	[4]
<b>Cu-Sb<sub>2</sub>O<sub>3</sub></b>	0.1 M KCl	-0.99	6.7	CO	[5]
<b>Sb-Cu<sub>2</sub>O derived bimetallic catalyst</b>	0.1 M KHCO <sub>3</sub>	-0.8 to -1.2	37.3 to 74.0	CO	[6]
<b>Single atom Sb on Cu</b>	0.5 M KHCO <sub>3</sub>	-0.97	150	CO	[7]
<b>Sulfide-derived Cu-Sb catalyst</b>					
<b>S-derived Cu-Sb</b>	1 M KHCO <sub>3</sub>	-1.0	37.6	CO	This work
<b>Other sulfide-derived catalysts</b>					
<b>S-modified Cu</b>	0.1 M KHCO <sub>3</sub>	-0.8	Trace	HCOOH	[8]
<b>CdS nanorods</b>	0.1 M KHCO <sub>3</sub>	-1.2	27.1	CO	[9]

### S3.5 ECSA

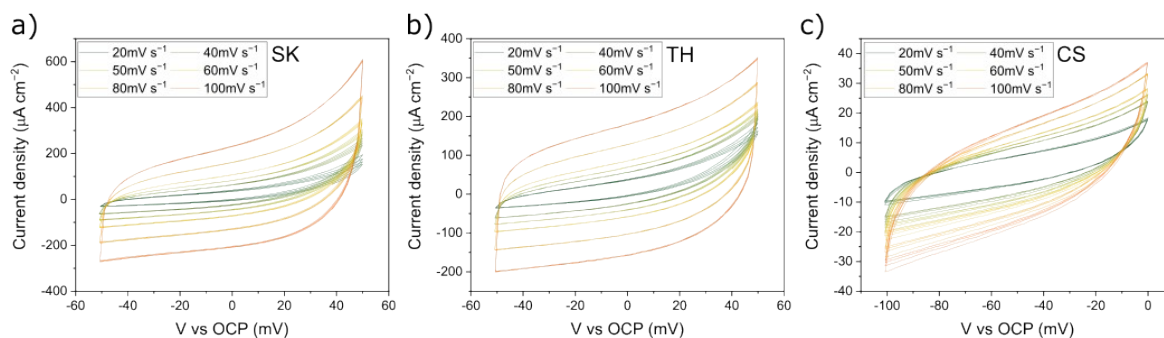


**Figure S8:** Cyclic voltammograms of the three catalyst samples done in non-Faradaic region for determination of electrochemically active surface area (ECSA). Catalysts were pre-reduced at 55mA/cm<sup>2</sup> prior to the test which was done on a 3mm diameter glassy carbon electrode.

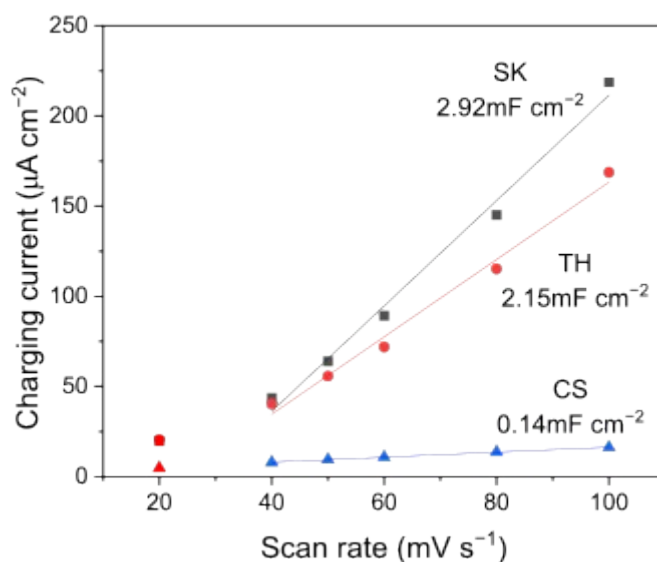


**Figure S9:** Charging current densities plotted against scan rate with double layer capacitance indicated for the three Cu-Sb-S catalysts. Catalysts were pre-reduced at 55mA/cm<sup>2</sup> prior to the test which was done on a 3mm diameter glassy carbon electrode.

## Section S4: Post-reduction characterization and remnant sulfur

### S4.1 CV

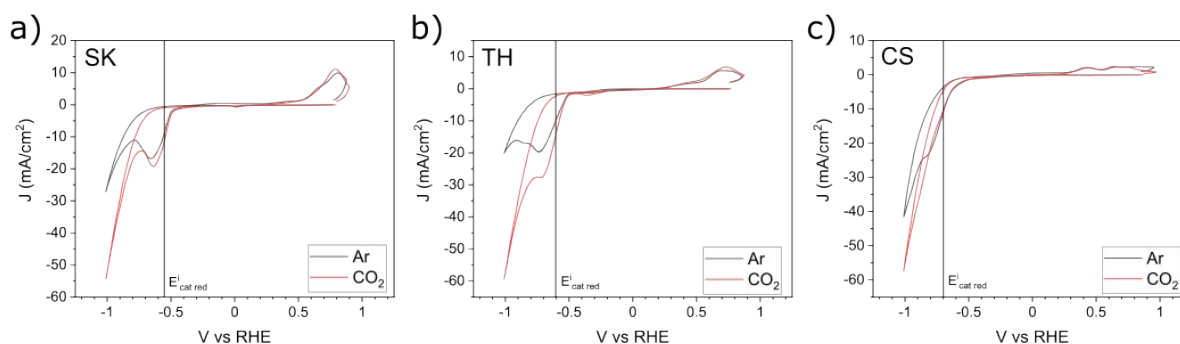


**Figure S10:** Cyclic voltammograms of the three catalyst samples done in Ar and CO<sub>2</sub>, with the catalyst reduction potential, which was obtained from the inflection point of the derivative, indicated.

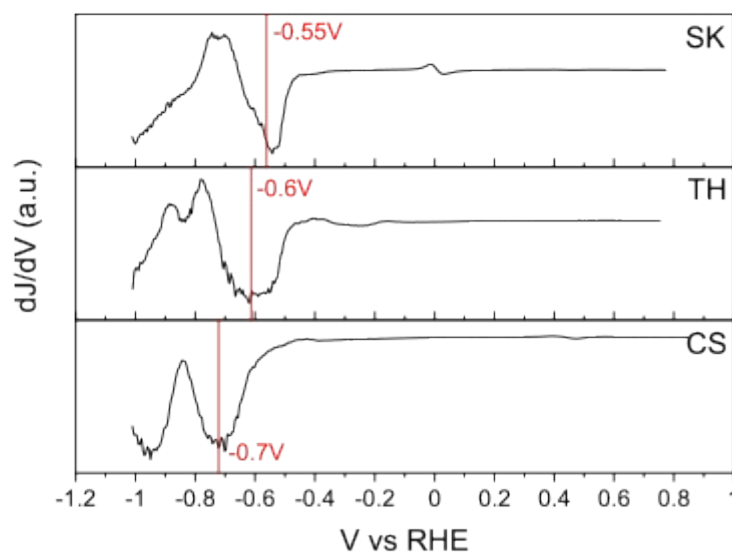


**Figure S11:** Derivative of cyclic voltammograms of the three catalyst samples with the value of the catalyst reduction potential indicated.

### S4.2 ICP of electrolyte

**Table S2:** ICP results of electrolyte for 9 $\times$  loading samples used for XRD.

Sample name	[Cu] (ppb)	[Sb] (ppb)
SK	16.8	75.8
TH	14.1	19.6
CS	16.9	12.6

### S4.3 EDX mapping after reduction

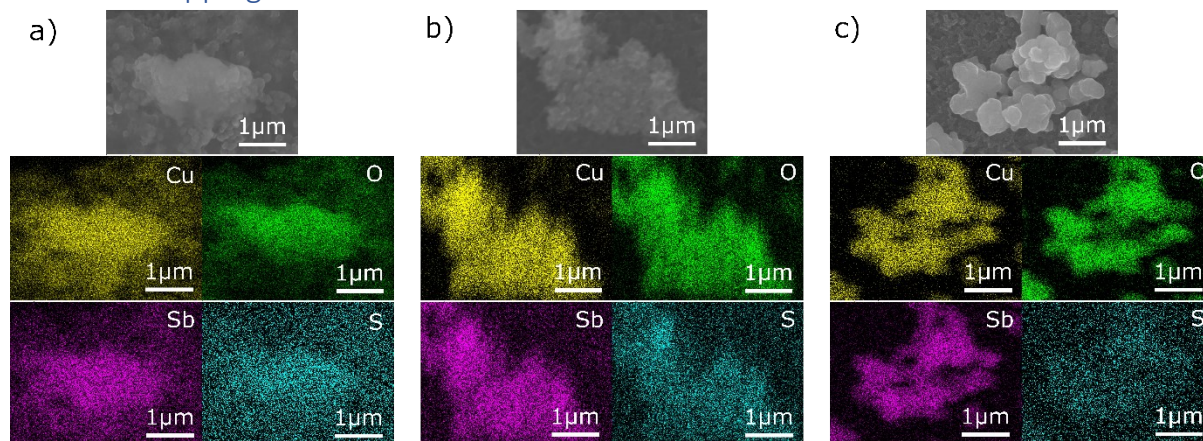


**Figure S12:** EDX mapping of the three catalyst samples on carbon paper after reduction at -1V vs RHE. a) SK b) TH c) CS

### S4.4 XPS peaks after reduction

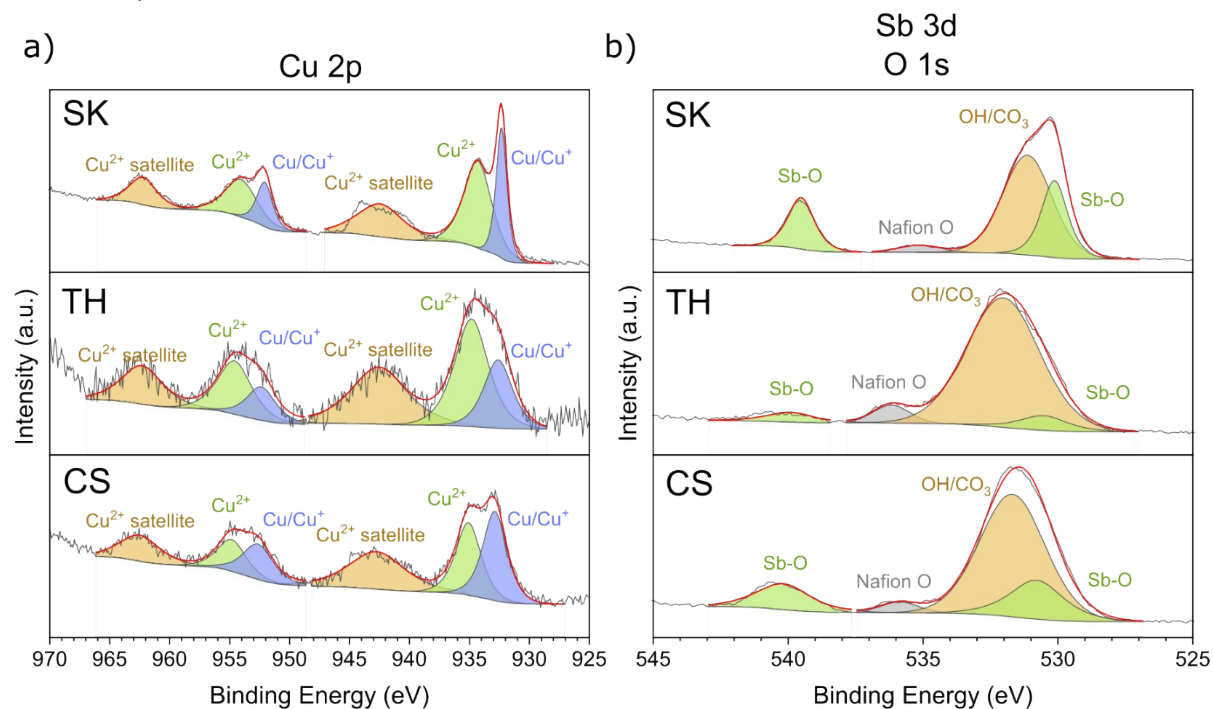


**Figure S13:** XPS peaks of the three catalyst samples on carbon paper after reduction at -1V vs RHE. a) Cu 2p peaks b) Sb 3d and O 1s peaks

#### S4.5 SAED after reduction

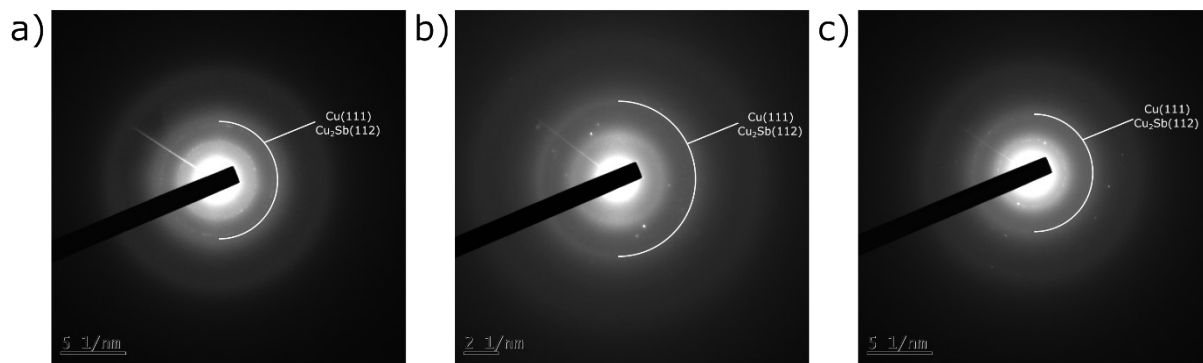


**Figure S14:** SAED images of samples scraped off carbon paper after reduction at -1V vs RHE, with the main peak of Cu(111) or Cu<sub>2</sub>Sb(112) indicated. a) SK b) TH c) CS

#### S4.6 SEM after reduction

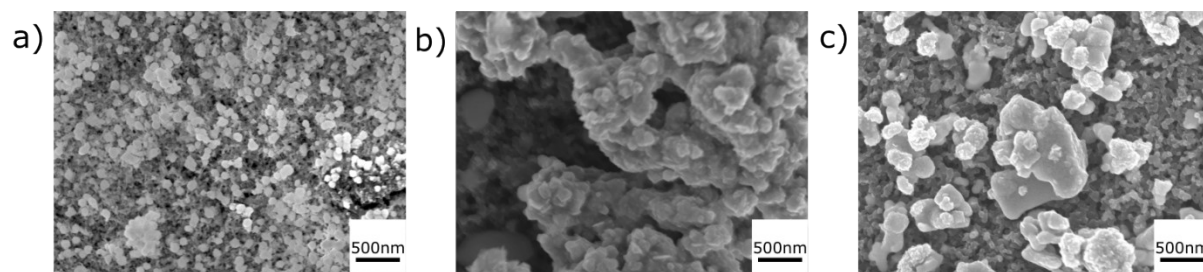


**Figure S15:** SEM images of the three catalyst samples on carbon paper after reduction at -1V vs RHE. a) SK b) TH c) CS

#### S4.7 TEM after reduction

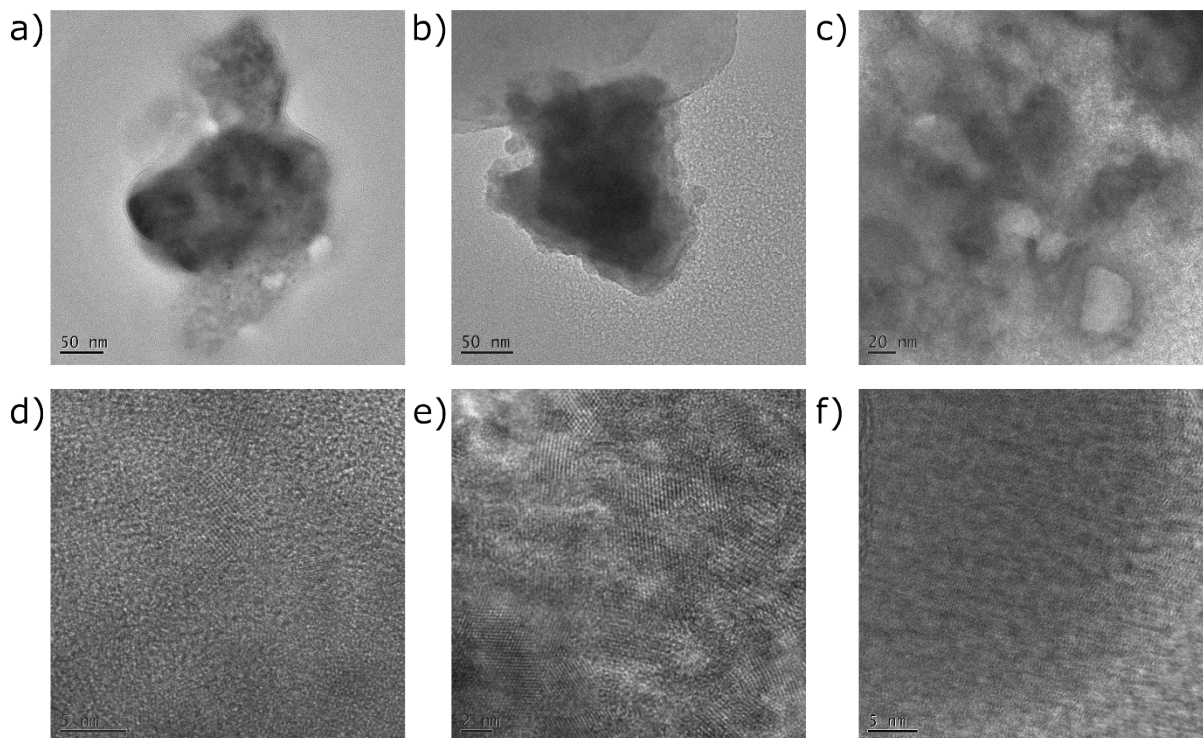


**Figure S16:** TEM images of samples scraped off carbon paper after reduction at -1V vs RHE. a) SK low magnification b) TH low magnification c) CS low magnification d)SK high magnification e) TH high magnification f) CS high magnification

S4.8 Phase diagram

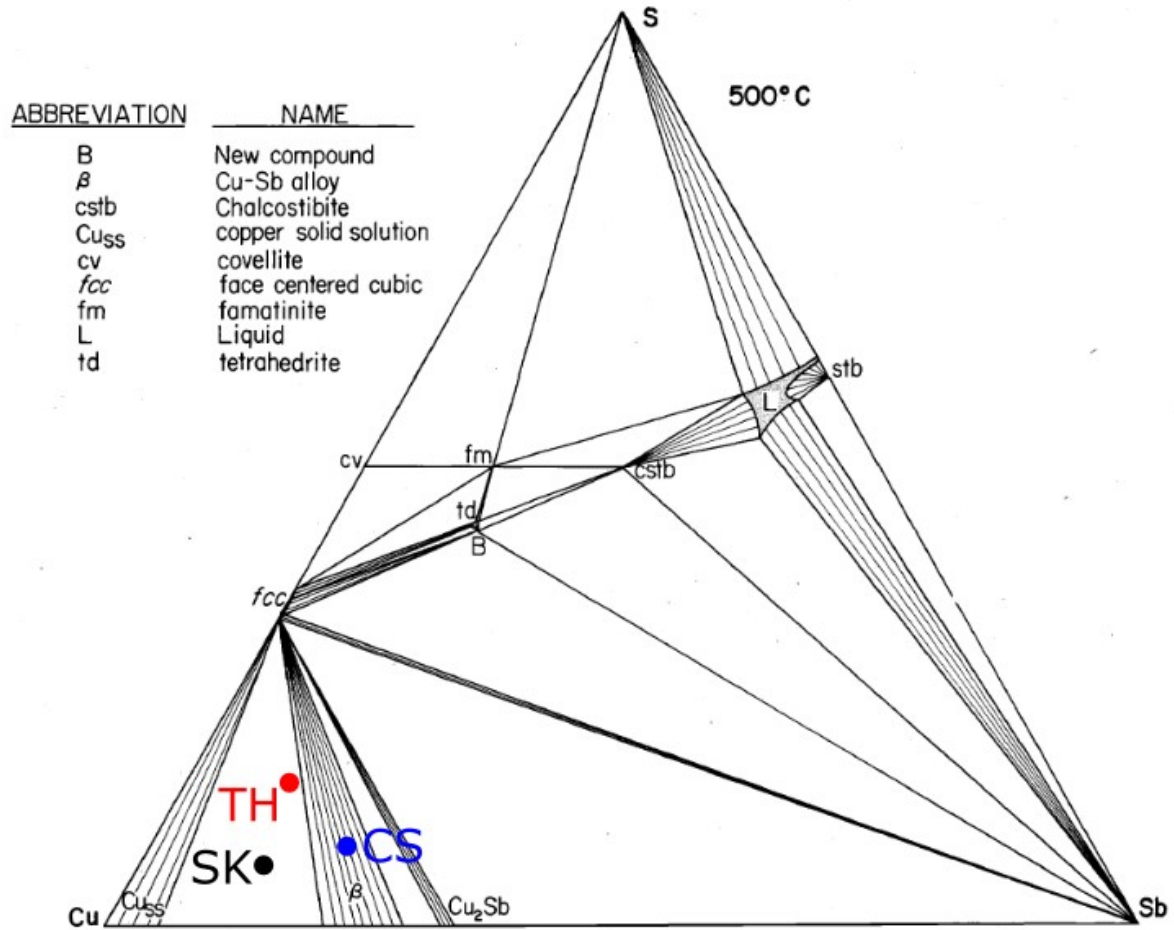


**Figure S17:** Elemental composition of samples after reduction plotted on Cu-Sb-S phase diagram taken from Skinner et al[10]

#### S4.9 Rietveld refinement of SK sample after reduction

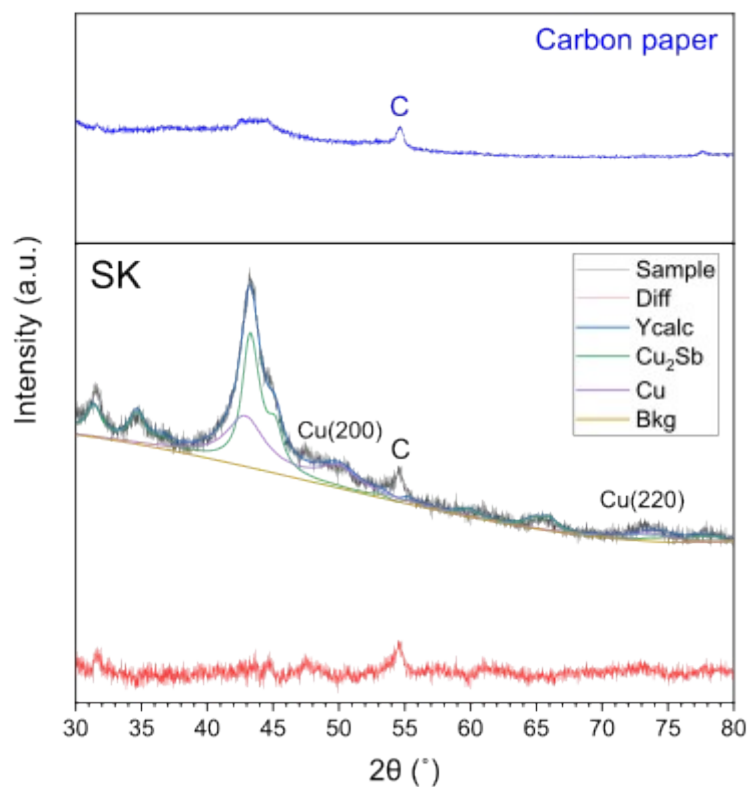


**Figure S18:** Rietveld refinement of the SK sample after reduction at -1V vs RHE for 9x loading. The peak labelled C is attributable to carbon paper. The refinement was done from 30° to 80° to exclude the carbon peak at 26.5° as well as a peak we could not identify as either Sb or Sb<sub>2</sub>O<sub>4</sub>.

**Table S3:** Parameters used in Rietveld refinement of SK sample after reduction at -1V vs RHE for 9x loading.

Phase	Wt%	a (Å)	c (Å)	Cry size (nm)	Rexp	Rwp	Rp	GOF
Cu <sub>2</sub> Sb	35.951	3.9925005	6.1525887	4.750	2.50	3.42	2.61	1.37
Cu	64.049	3.6298331		1.762				

## Section S5: DFT calculations

### S5.1 Atomic structures of sulfur-decorated $\text{Cu}_2\text{Sb}(100)$ systems

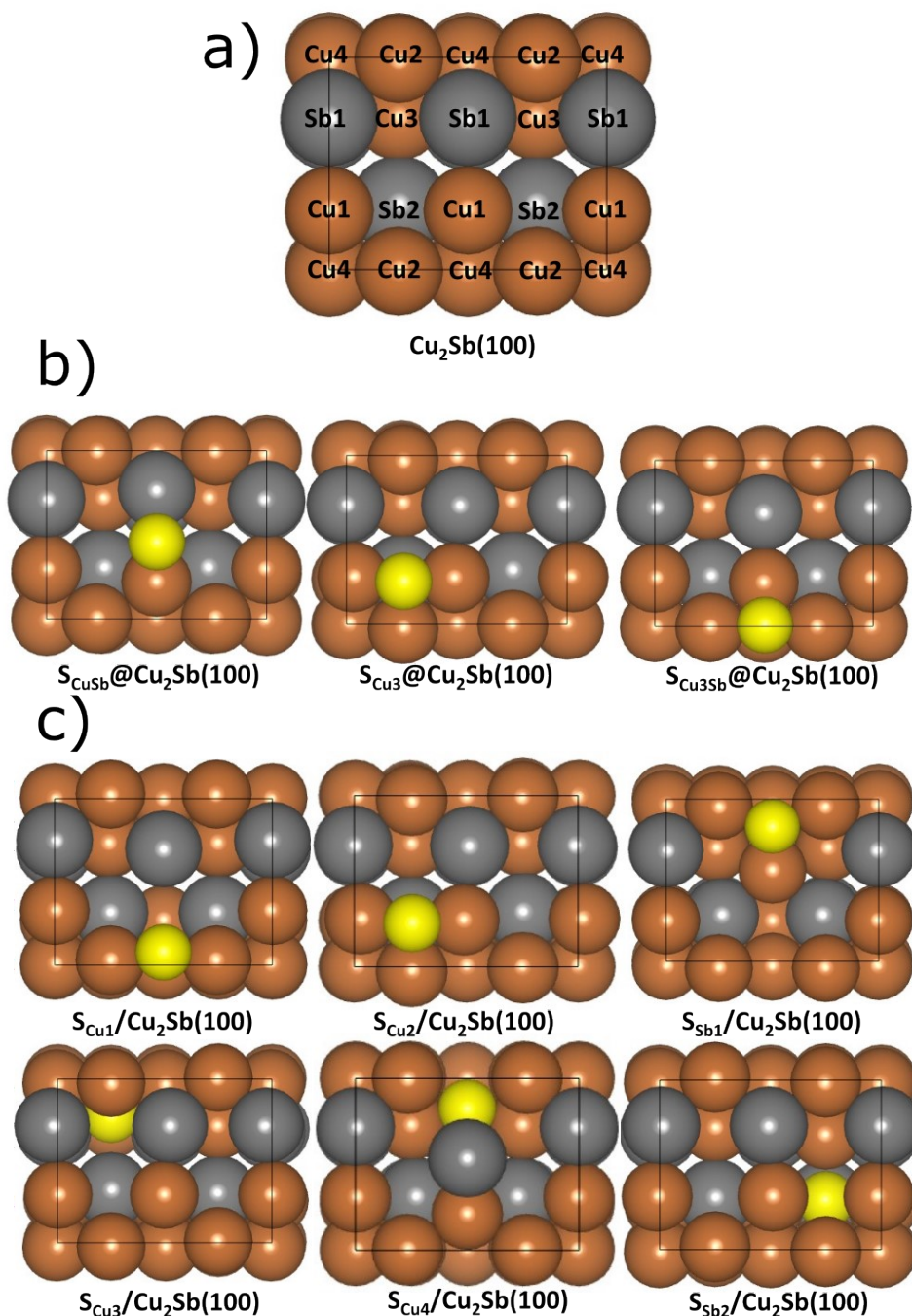


**Figure S19:** Adsorption and substitutional sites for a S atom considered. (a) The clean pristine  $\text{Cu}_2\text{Sb}(100)$  surface showing all symmetry inequivalent substitutional sites for a sulfur atom dopant. Note that Cu1, Cu2 and Sb1 sites in the topmost atomic layer while Cu3, Cu4 and Sb2 sites are in the next atomic layer, giving a total of six possible sites. (b) The three various adsorption configurations for a sulfur adatom on the bridge, threefold- $\text{Cu}_3$  and fourfold  $\text{Cu}_3\text{Sb}$  sites, respectively. (c) The six substitutional sulfur atom dopant cases. The subscript in each notation denotes the adsorption or substitutional sites for a S atom.

## S5.2 Sulfur Stability Analysis

The energy penalty ( $\Delta E$ ) of forming a sulfur vacancy in each primitive cell of TH, CS and SK is calculated using equation S1.

$$\Delta E = E_{final} - E_{initial} - E_{S(g)} \quad \#(Equation\ S1)$$

where  $E_{initial}$  and  $E_{final}$  refer to the electronic energy of the primitive cell of a parent phase with and without a single S atom vacancy respectively, and  $E_{S(g)}$  refers to the electronic energy of a single S atom in the gas phase.

The stability of Cu and Sb point defects mentioned in the main text was evaluated using the formation energy ( $\Delta_{form}E$ ), which is defined in equation S2.

$$\Delta_{form}E = E_{\square defect} - E_{Cu_2Sb(100)} + n_S E_{S(g)} + n_{Cu} E_{fcc - Cu(s)} + n_{Sb} E_{tri - Sb(s)} \quad \#(Equation\ S2)$$

where  $E_{\square defect}$ , and  $E_{Cu_2Sb(100)}$  refer to the electronic energy of the configuration of interest and the pristine Cu<sub>2</sub>Sb(100) surface.  $E_{S(g)}$ ,  $E_{fcc - Cu(s)}$  and  $E_{tri - Sb(s)}$  refer to the electronic energy of a single gas-phase S atom, Cu atom in the bulk primitive face-centered cubic crystal (space group:  $Fm\bar{3}m$ ), and an Sb atom in the bulk primitive trigonal crystal (space group:  $R\bar{3}m$ ), respectively.  $n_S$ ,  $n_{Cu}$  and  $n_{Sb}$  represent the number of S, Cu and Sb atoms removed or added to the system. Positive (negative) integers implying atoms added (removed).

To gauge the stability of sulfur doped systems, the desorption energy to form H<sub>2</sub>S ( $\Delta E_{H_2S}$ ) is used as a stability metric, which is calculated using equation S3.

$$\Delta E_{H_2S} = E_* + E_{H_2S(g)} - E_{S^*} - E_{H_2(g)} \quad \#(Equation\ S3)$$

where  $E_*$ ,  $E_{H_2S(g)}$  and  $E_{H_2(g)}$  represent the electronic energy of the surface site, an isolated H<sub>2</sub>S molecule and an isolated H<sub>2</sub> molecule, respectively. In the equation used for calculating  $\Delta E_{H_2S}$ , the  $E_*$  for S adatoms refers to the electronic energy of Cu<sub>2</sub>Sb (100). For the S dopant in the topmost atomic layer,  $E_*$  refers to the electronic energy of Cu<sub>2</sub>Sb (100) containing an S atom vacancy.

Figure S19(b) shows three different adsorption sites for a sulfur adatom: (1) Cu-Sb bridge site ( $S_{CuSb}@Cu_2Sb(100)$ ), (2) threefold Cu-Cu-Cu hollow site ( $S_{Cu3}@Cu_2Sb(100)$ ) and the (3) fourfold Cu-Cu-Cu-Sb hollow site ( $S_{Cu3Sb}@Cu_2Sb(100)$ ). Substitutionally doped sulfur is considered in the two topmost atomic layers, giving a total of six symmetrical inequivalent doping configurations as portrayed in Figure S19(c). These configurations are labelled as Cu1, Cu2 and Sb1 in the topmost atomic layer and Cu3, Cu4 and Sb2 in the next atomic layer. The stability of the S atoms in the systems was evaluated with the formation energy ( $\Delta_{form}E$ ) and the desorption energy of S as H<sub>2</sub>S ( $\Delta E_{H_2S}$ ) according to equations S2 and S3 respectively as tabulated in Table S3.

With S adatom on the hollow site of Cu(111) (abbreviated as  $S_{Cu3}@Cu(111)$ ) as the reference system ( $\Delta E_{H_2S} = +1.14$  eV), we compared the stability of the various sulfur modified sites. This is because prior experimental and computational studies have indicated that S\* remains stable on Cu (111) under CO<sub>2</sub>RR working potentials from -0.6 V to -0.8 V vs RHE.[11] All three S adatom configurations on Cu<sub>2</sub>Sb are less stable than S adatoms on Cu(111). Hence S adatoms are less likely to adsorb on Cu<sub>2</sub>Sb(100) during the operating condition of -1.0 eV. Since  $\Delta E_{H_2S}$  for  $S_{CuSb}@Cu_2Sb(100)$  is at least around 0.6 eV

more positive than that for the other two adsorption configuration,  $S_{CuSb}@Cu_2Sb(100)$  was not considered in further analyses. The S atom substitutionally doped at the copper sites in the topmost atomic layer (i.e.,  $S_{Cu1}/Cu_2Sb(100)$ ,  $S_{Cu2}/Cu_2Sb(100)$ ) also showed poorer stability than  $S^*$  on Cu (111). However, S substituting at the Sb site in topmost atomic layer (i.e.  $S_{Sb1}/Cu_2Sb(100)$ ) is more stable than  $S_{Cu3}@Cu(111)$  by 0.59 eV.

**Table S4. Formation energies of the sulfur-decorated ( $\Delta_{form}E_{S^*}$ ) and vacancy ( $\Delta_{form}E_V$ ) surface motifs and desorption energies of the sulfur in sulfur-decorated systems as  $H_2S$  ( $\Delta E_{H_2S}$ ).**

	$\Delta_{form}E_{S^*/V} / \text{eV}$	$\Delta E_{H_2S} / \text{eV}$
<b><math>S_{Cu3}@Cu(111)</math>, reference</b>	-4.60	+1.14
<b><math>S_{CuSb}@Cu_2Sb(100)</math></b>	-3.80	+0.34
<b><math>S_{Cu3}@Cu_2Sb(100)</math></b>	-4.46	+1.00
<b><math>S_{Cu3Sb}@Cu_2Sb(100)</math></b>	-4.39	+0.93
<b><math>S_{Cu1}/Cu_2Sb(100)</math></b>	-4.45	+0.79
<b><math>S_{Cu2}/Cu_2Sb(100)</math></b>	-4.11	+0.80
<b><math>S_{Sb1}/Cu_2Sb(100)</math></b>	-4.14	+1.73
<b><math>S_{Cu3}/Cu_2Sb(100)</math></b>	-2.66	-0.99
<b><math>S_{Cu4}/Cu_2Sb(100)</math></b>	-3.25	-0.05
<b><math>S_{Sb2}/Cu_2Sb(100)</math></b>	-3.34	+0.93
<b><math>V_{Cu1}/Cu_2Sb(100)</math></b>	-0.20	-
<b><math>V_{Cu2}/Cu_2Sb(100)</math></b>	+0.16	-
<b><math>V_{Sb1}/Cu_2Sb(100)</math></b>	+1.05	-

When an S atom desorbs from the surface as  $H_2S$ , it inevitably leaves behind a vacancy. For instance, the S atom in  $S_{Cu1}/Cu_2Sb(100)$  desorbs as  $H_2S$  leaving a  $V_{Cu1}/Cu_2Sb(100)$  vacancy structure. Correspondingly,  $S_{Cu2}/Cu_2Sb(100)$  forms the  $V_{Cu2}/Cu_2Sb(100)$  structure and  $S_{Sb1}/Cu_2Sb(100)$  forms the  $V_{Sb1}$ . The formation energy of the three vacancy sites trend as  $V_{Cu1}/Cu_2Sb(100) > V_{Cu2}/Cu_2Sb(100) > V_{Sb1}/Cu_2Sb(100)$ , with the formation of  $V_{Cu1}/Cu_2Sb(100)$  being most thermodynamically favoured. We also predict that  $V_{Sb1}/Cu_2Sb(100)$  is unlikely to form, since  $S_{Sb1}/Cu_2Sb(100)$  is predicted to be stable during operating conditions and the  $\Delta_{form}E_V$  value for  $V_{Sb1}$  at least 1.0 eV more positive than that for  $V_{Cu1}/Cu_2Sb(100)$  and  $V_{Cu2}/Cu_2Sb(100)$ . Hence, we include  $V_{Cu1}/Cu_2Sb(100)$  and  $V_{Cu2}/Cu_2Sb(100)$  in our analysis of selectivity and reactivity trends towards 2e- $CO_2RR$ . As a limiting case of a restructured surface, we also consider the  $Cu_2Sb(101)$  stepped surface.

For the substitutionally doped sulfur in the second atomic layer ( $S_{Cu3}/Cu_2Sb(100)$ ,  $S_{Cu4}/Cu_2Sb(100)$  and  $S_{Sb2}/Cu_2Sb(100)$ ) to desorb as  $H_2S$ , the sulfur atom must first diffuse through the solid to the surface before it can be hydrogenated. The vacancy is thus created in the topmost layer. For a fair comparison of  $\Delta E_{H_2S}$ , we assume the most stable  $V_{Cu1}/Cu_2Sb(100)$  as the vacancy structure after  $H_2S$  desorption. While the three configurations gave  $\Delta E_{H_2S}$  values that are less positive than  $S_{Cu3}@Cu(111)$ , the S atom must first diffuse through the solid to the surface before it can be hydrogenated. This diffusion process is likely activated, hence S atoms in the second atomic layer could be kinetically stabilised during the operating conditions.



### S5.3 Additional Computational Details on the Computational Hydrogen Electrode Approach

The catalytic activity of the surface models was analysed using the computational hydrogen electrode approach[12], in which the electrochemical potential of a proton–electron pair,  $\tilde{\mu}(\text{H}^+ + e^-)$ , is related to the chemical potential of  $\text{H}_2$  at ambient conditions (278.25 K, 1 atm, 0 V),  $\mu_{\text{H}_2}$ , and the operating potential vs. RHE,  $U$ , according to equation S4:

$$\tilde{\mu}_{(\text{H}^+ + e^-)} = \frac{1}{2}\mu_{\text{H}_2}(278.15 \text{ K}, 1 \text{ atm}, 0 \text{ V}) - eU \text{ \#(Equation S4)}$$

where  $e$  is the elementary charge. The potential-dependent Gibbs energy change ( $\Delta_r G(U)$ ) for any reaction can be estimated using equation S5:

$$\Delta_r G(U) = \Delta E_{ele} + \Delta E_{ZP} + \Delta \int C_p dT + T\Delta S + \Delta E_{sol} - neU \text{ \#(Equation S5)}$$

where  $\Delta E_{ZPC}$  is the change in zero-point energy,  $\Delta \int C_p dT$  is the change in enthalpic temperature correction,  $T$  is the temperature,  $\Delta S$  is the entropy change,  $\Delta E_{sol}$  is the solvation energy and  $n$  is the number of electrons transferred. We adopted the value of these terms as already evaluated in Tang et al.[13] as tabulated in Table S6.

We evaluated the catalytic performance in two parts. We studied the selectivity towards electrocatalytic CO or formate formation pathways. We then analysed trends in electrochemical barriers from the free energy diagrams.

## S5.4 Adsorption metrics analysis

The adsorption energies of CO<sub>2</sub> reduction reaction intermediates like H\* ( $\Delta_{ads}G_{H^*}$ ), HCOO\* ( $\Delta_{ads}G_{HCOO^*}$ ), COOH\* ( $\Delta_{ads}G_{COOH^*}$ ) and CO\* ( $\Delta_{ads}G_{CO^*}$ ) were calculated using H<sub>2</sub>, H<sub>2</sub>O and CO<sub>2</sub> as reference states for H-, O- and C-containing species as shown in equations S6 – S9. To minimize the error in the gas phase energy calculations using the PBE functional as reported by Peterson et al., we corrected the Gibbs energy of CO, CO<sub>2</sub>, H<sub>2</sub> and H<sub>2</sub>O by -0.51, +0.13, -0.08 and 0.06 eV, respectively.[14]

As such, the potential dependent adsorption Gibbs energies of H\*, HCOO\*, COOH\* and CO\* are given by equations S6 – S9:

$$\Delta_{ads}G_{H^*}(U) = G_{H^*} - \frac{1}{2}G_{H_2} - G_* + eU \#(\text{Equation S6})$$

$$\Delta_{ads}G_{HCOO^*}(U) = G_{HCOO^*} - G_{CO_2} - \frac{1}{2}G_{H_2} - G_* + eU \#(\text{Equation S7})$$

$$\Delta_{ads}G_{COOH^*}(U) = G_{COOH^*} - G_{CO_2} - \frac{1}{2}G_{H_2} - G_* + eU \#(\text{Equation S8})$$

$$\Delta_{ads}G_{CO^*}(U) = G_{CO^*} + G_{H_2O} - G_{CO_2} - G_{H_2} - G_* + 2eU \#(\text{Equation S9})$$

The 11 models that were considered further besides the reference Cu<sub>2</sub>Sb(100) are the two S adatom structures, (i) S<sub>Cu3</sub>@Cu<sub>2</sub>Sb(100) and (ii) S<sub>Cu3Sb</sub>@Cu<sub>2</sub>Sb(100); three structures with S as a dopant in the topmost atomic layer, (iii) S<sub>Cu1</sub>/Cu<sub>2</sub>Sb(100), (iv) S<sub>Cu2</sub>/Cu<sub>2</sub>Sb(100) and (v) S<sub>Sb1</sub>/Cu<sub>2</sub>Sb(100), three structures with S as a dopant in the second topmost atomic layer, (vi) S<sub>Cu3</sub>/Cu<sub>2</sub>Sb(100), (vii) S<sub>Cu4</sub>/Cu<sub>2</sub>Sb(100) and (viii) S<sub>Sb2</sub>/Cu<sub>2</sub>Sb(100), two vacancy structures, (ix) V<sub>Cu1</sub>/Cu<sub>2</sub>Sb(100) and (x) V<sub>Cu2</sub>/Cu<sub>2</sub>Sb(100) and lastly (xi) Cu<sub>2</sub>Sb(101).

**Table S5. Adsorption Gibbs energy for key intermediates i.e., H\*, COOH\*, HCOO\* and CO\*, involved in 2e-CO<sub>2</sub>RR**

Surface Structure	$\Delta_{ads}G_{H^*} / \text{eV}$	$\Delta_{ads}G_{COOH^*} / \text{eV}$	$\Delta_{ads}G_{HCOO^*} / \text{eV}$	$\Delta_{ads}G_{CO^*} / \text{eV}$
<b>Cu(111)</b>	-0.17	0.58	-0.45	0.17
<b>Cu<sub>2</sub>Sb(100), reference</b>	-0.05	0.66	0.09	0.17
<b>S<sub>Cu3</sub>@Cu<sub>2</sub>Sb(100)</b>	<b>0.08</b>	<b>0.70</b>	<b>0.44</b>	<b>0.21</b>
<b>S<sub>Cu3Sb</sub>@Cu<sub>2</sub>Sb(100)</b>	<b>0.14</b>	<b>0.85</b>	<b>0.38</b>	<b>0.31</b>
<b>S<sub>Cu1</sub>/Cu<sub>2</sub>Sb(100)</b>	<b>0.22</b>	<b>0.96</b>	<b>0.54</b>	<b>0.43</b>
<b>S<sub>Cu2</sub>/Cu<sub>2</sub>Sb(100)</b>	<b>0.09</b>	<b>0.73</b>	<b>0.47</b>	<b>0.19</b>
<b>S<sub>Sb1</sub>/Cu<sub>2</sub>Sb(100)</b>	<b>0.06</b>	<b>0.77</b>	<b>0.21</b>	<b>0.18</b>
<b>V<sub>Cu1</sub>/Cu<sub>2</sub>Sb(100)</b>	<b>0.02</b>	-0.22	<b>0.14</b>	0.11
<b>V<sub>Cu2</sub>/Cu<sub>2</sub>Sb(100)</b>	-0.08	<b>0.75</b>	<b>0.25</b>	<b>0.21</b>
<b>S<sub>Cu3</sub>/Cu<sub>2</sub>Sb(100)</b>	-0.20	0.12	-0.24	0.06
<b>S<sub>Cu4</sub>/Cu<sub>2</sub>Sb(100)</b>	-0.20	0.58	-0.27	-0.26
<b>S<sub>Sb2</sub>/Cu<sub>2</sub>Sb(100)</b>	<b>0.01</b>	0.29	-0.14	0.28
<b>Cu<sub>2</sub>Sb(101)</b>	-0.84	0.50	-0.50	-0.05

The adsorption Gibbs energy is calculated using DFT-derived electronic energies and the correction terms in Table S6. Values which are in bold and italics are more positive than that of the reference Cu<sub>2</sub>Sb(100).

We determined the most stable adsorption sites of H\*, COOH\*, HCOO\* and CO\* on all Cu<sub>2</sub>Sb-based structures with the adsorption energies shown in Table S4. The Cu-Cu bridge site is the most stable adsorption site for H\* and CO\*. COOH\* and HCOO\* adopted  $\eta^2(\text{C},\text{O})$  and  $\eta^2(\text{O},\text{O})$  adsorption configurations on two adjacent Cu atoms. These adsorption configurations are shown in Figure S20. We first compare adsorption energies of reaction intermediates on our reference surface, Cu<sub>2</sub>Sb(100), against that on a prototypical CO<sub>2</sub>RR catalyst, Cu(111). We note that alloying of Sb into Cu as Cu<sub>2</sub>Sb(100) results in negligible change in CO\* adsorption strength while the adsorption strength of H\*, COOH\* and HCOO\* decreases.

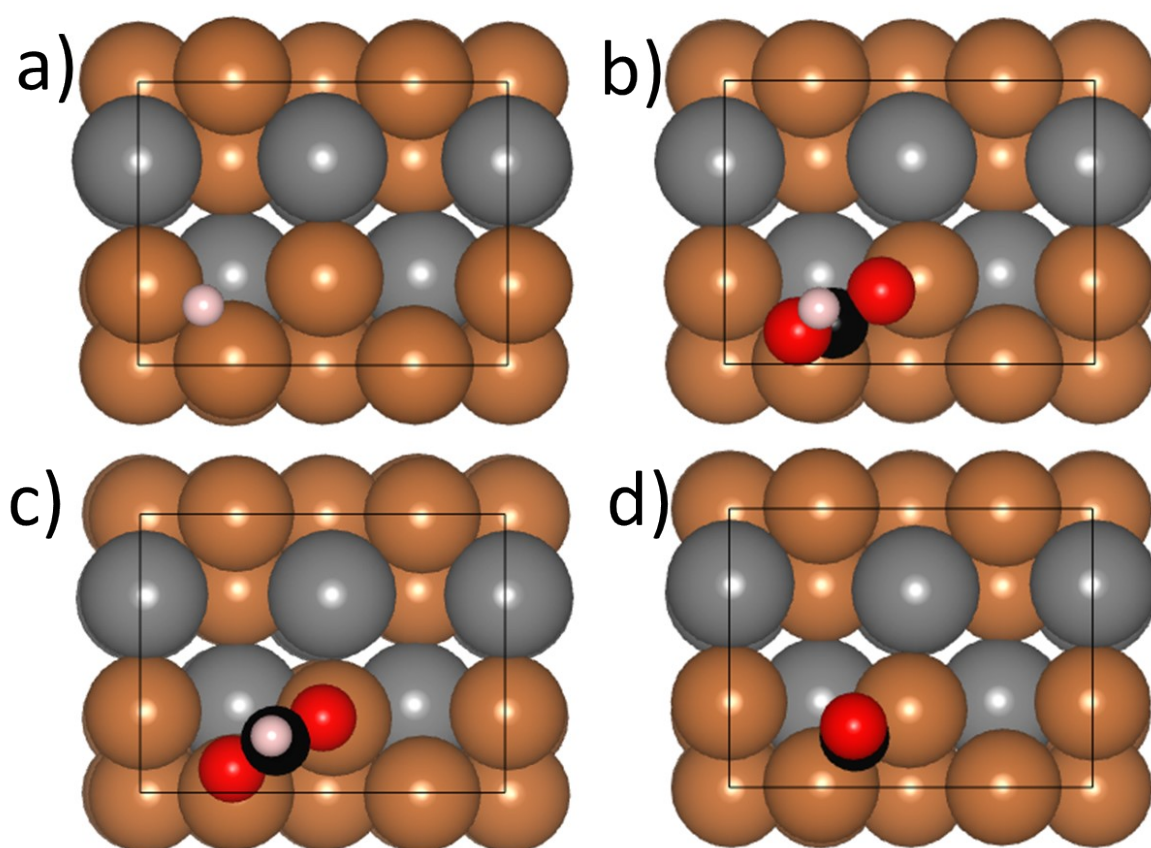


**Figure S20.** Adsorption configurations of the key intermediates i.e., (a) \*H, (b) \*COOH, (c) HCOO\* and (d) \*CO, involved in 2e-CO<sub>2</sub>RR.

We then compare the adsorption energies on all surfaces in Table S4 against those on Cu<sub>2</sub>Sb(100). Note that values bolded and italicized are more positive than the corresponding ones for Cu<sub>2</sub>Sb(100). Similar adsorption configurations of intermediates are obtained across sulfur-modified Cu sites, Cu vacancies, and Cu<sub>2</sub>Sb(101). From Table S4, one can dichotomize the set of surface models into two group in terms of adsorption energies. Generally, sulfur as an adatom or as a substitutional dopant in the topmost layer and in vacancy structures weakened the binding strength of the adsorbates relative to Cu<sub>2</sub>Sb(100). Sulfur dopants in the

second atomic layer and  $\text{Cu}_2\text{Sb}$  (101) enhanced the binding of adsorbates relative to  $\text{Cu}_2\text{Sb}(100)$ . More importantly, eight surfaces, i.e.,  $S_{\text{Cu}_3@}\text{Cu}_2\text{Sb}(100)$ ,  $S_{\text{Cu}_3\text{Sb}@}\text{Cu}_2\text{Sb}(100)$ ,  $S_{\text{Cu}_1}/\text{Cu}_2\text{Sb}(100)$ ,  $S_{\text{Cu}_2}/\text{Cu}_2\text{Sb}(100)$ ,  $S_{\text{Sb}_1}/\text{Cu}_2\text{Sb}(100)$ ,  $S_{\text{Sb}_2}/\text{Cu}_2\text{Sb}(100)$ ,  $V_{\text{Cu}_2}/\text{Cu}_2\text{Sb}(100)$  bind  $\text{CO}^*$  less strongly than both  $\text{Cu}$  (111) and  $\text{Cu}_2\text{Sb}$  (100). It has been demonstrated that  $\text{CO}_2\text{RR}$  catalysts that are selective towards the 2e products experimentally possess a  $\text{CO}^*$  binding energy that is weaker than that on  $\text{Cu}(111)$ . [13, 15]

The weaker binding of  $\text{CO}^*$  on the eight surfaces will promote  $\text{CO}^*$  desorption rather than further reduction to  $\text{CHO}^*$  or  $\text{COH}^*$ . Since the CS, SK and TH samples showed a high selectivity towards the 2e- $\text{CO}_2\text{RR}$  products even at a more negative applied voltage of -1.2 V, these eight active site motifs are more likely to be present in the catalytic active Cu-Sb-S phases.

### S5.5 2e<sup>-</sup> CO<sub>2</sub>RR and HER catalytic activity analysis

We adopted a similar approach by Tang et al. to evaluate the selectivity of the 2e-CO<sub>2</sub>RR products (i.e., CO and HCOOH).[13] It has been well-accepted that the formation of COOH\* occurs via the electrochemical hydrogenation of a CO<sub>2</sub>. The driving force for COOH\* formation as a function of the applied potential is given by  $\Delta_{ads}G_{COOH^*}(U)$  as in equation S10:

$$\Delta_{R1}G(CO_2(g) + * + H^+ + e^- \rightarrow COOH^*) = \Delta_{ads}G_{COOH^*}(U) \#(Equation\ S10)$$

HCOO\* occurs from the chemical step involving CO<sub>2</sub> and H\*, whose formation is unaffected by the applied potential and is governed by equation S11:

$$\Delta_{R2}G(CO_2(g) + H^* \rightarrow HCOO^*) = \Delta G_{HCOO^*}(U) - \Delta G_{H^*}(U) \#(Equation\ S11)$$

Equation S12 is also required to describe the availability of H\* for the formation of HCOO\*:

$$\Delta_{R3}G(* + H^+ + e^- \rightarrow H^*) = \Delta G_{H^*}(U) \#(Equation\ S12)$$

Essentially, a product is more selective at a specific operating potential if the thermodynamic driving force to produce the relevant intermediate (COOH\* or HCOO\*) from the reactant species is larger. One can then use  $\Delta_{R1}G - \Delta_{R2}G$  as a descriptor for determining the selectivity of a given active site motif towards either CO or formate. A more negative (positive) value indicates a larger driving force for the CO (formate) pathway.

To plot the potential energy diagrams, the 2e-CO<sub>2</sub>RR pathway forming CO considered is given by S13 – S15 while that forming formate as HCOOH is given by S16 – S18:

$$CO_2(g) + * + (H^+ + e^-) \rightarrow COOH^* (\Delta_{C1}G) \#(Equation\ S13)$$

$$COOH^* + (H^+ + e^-) \rightarrow CO^* + H_2O (\Delta_{C2}G) \#(Equation\ S14)$$

$$CO^* \rightarrow CO + * (\Delta_{C3}G) \#(Equation\ S15)$$

$$* + (H^+ + e^-) \rightarrow H^* (\Delta_{F1}G) \#(Equation\ S16)$$

$$CO_2 + H^* \rightarrow HCOO^* (\Delta_{F2}G) \#(Equation\ S17)$$

$HCOO^* + (H^+ + e^-) \rightarrow HCOOH + * (\Delta_{F3}G) \#(Equation\ S18)$  In addition, hydrogen evolution reaction (HER) is considered to proceed via S19 – S20:

$$* + (H^+ + e^-) \rightarrow H^* (\Delta_{H1}G) \#(Equation\ S19)$$

$H^* + (H^+ + e^-) \rightarrow H_2 + * (\Delta_{H2}G) \#(Equation\ S20)$  The Gibbs energy changes for the CO, formate and HER pathways at 0.0 V are given in Table S6, S7 and S8 respectively.

## S5.6 Other DFT data

**Table S6: DFT-calculated surface energies.** The description of the orthogonal, asymmetric slabs of different Cu<sub>2</sub>Sb facets encompassing only the primitive surface cell used in terms of slab thickness, constraints on the slab, lateral lattice parameters (*a* and *b*), surface area per primitive surface cell and surface energy.

Facet	Termination	Total no. of layers	No. of fixed layers	<i>a</i> / Å	<i>b</i> / Å	Surface Area / Å <sup>2</sup>	Surface energy / J m <sup>-2</sup>
(100)	Cu,Sb	6	2	3.98	6.09	24.12	2.38
(110)	Cu,Sb	6	2	5.63	6.09	34.28	2.48
(110)	Cu	6	2	5.63	6.09	24.28	2.44
(101)	Cu,Sb	9	3	7.28	3.98	28.95	2.67
(001)	Cu,Sb	9	3	3.97	3.97	15.76	3.28

**Table S7. Gas-phase and adsorbate Gibbs energy correction.** Contributions to the Gibbs energy of gas-phase and adsorbate species from zero-point energy ( $E_{zp}$ ), enthalpic temperature correction ( $J C_p dT$ ), entropic contribution ( $-TS$ ) and solvation correction involved in 2e-CO<sub>2</sub>RR pathway.

Species	$E_{zp}$ / eV	$J C_p dT$ / eV	$-TS$ / eV	$E_{sol}$ / eV
CO	0.13	0.09	-0.67	-
CO <sub>2</sub>	0.31	0.10	-0.67	-
HCOOH	0.90	0.11	-0.99	-
H <sub>2</sub>	0.27	0.09	-0.44	-
H <sub>2</sub> O	0.57	0.10	-0.67	-
HCOO*	0.61	0.06	-0.12	0.00
COOH*	0.62	0.09	-0.17	-0.25
H*	0.13	0.01	-0.02	0.00
CO*	0.17	0.07	-0.16	-0.10

**Table S8. Selectivity metrics at operating voltage of -1.0 V for Cu(111) and all 12 Cu<sub>2</sub>Sb-based surface motifs.**  $\Delta_{R1}G$  and  $\Delta_{R2}G$  govern the driving force for COOH\* and HCOO\* formation respectively. A positive (negative) value of  $\Delta_{R1}G - \Delta_{R2}G$  would favour CO (formate). The  $\Delta_{R3}G$  is used as a descriptor to define surface hydrogenation. A negative  $\Delta_{R3}G$  value favours surface hydrogenation.

Surface Structure	$\Delta_{R1}G$ / eV	$\Delta_{R2}G$ / eV	$\Delta_{R1}G - \Delta_{R2}G$ / eV	$\Delta_{R3}G$ / eV
<b>Cu(111)</b>	-0.42	-0.28	-0.15	-1.17
<b>Cu<sub>2</sub>Sb(100)</b>	-0.34	0.14	-0.48	-1.05
<b>S<sub>Cu3</sub>@Cu<sub>2</sub>Sb(100)</b>	-0.30	0.36	-0.66	-0.92
<b>S<sub>Cu3Sb</sub>@Cu<sub>2</sub>Sb(100)</b>	-0.15	0.24	-0.39	-0.86
<b>S<sub>Cu1</sub>/Cu<sub>2</sub>Sb(100)</b>	-0.04	0.32	-0.36	-0.78
<b>S<sub>Cu2</sub>/Cu<sub>2</sub>Sb(100)</b>	-0.27	0.38	-0.65	-0.91
<b>S<sub>Sb1</sub>/Cu<sub>2</sub>Sb(100)</b>	-0.23	0.15	-0.38	-0.94
<b>S<sub>Cu3</sub>/Cu<sub>2</sub>Sb(100)</b>	-0.88	-0.03	-0.85	-1.20
<b>S<sub>Cu4</sub>/Cu<sub>2</sub>Sb(100)</b>	-0.42	-0.08	-0.35	-1.20
<b>S<sub>Sb2</sub>/Cu<sub>2</sub>Sb(100)</b>	-0.71	-0.15	-0.56	-0.99
<b>V<sub>Cu1</sub>/Cu<sub>2</sub>Sb(100)</b>	-1.22	0.13	-1.34	-0.98
<b>V<sub>Cu2</sub>/Cu<sub>2</sub>Sb(100)</b>	-0.25	0.33	-0.58	-1.08
<b>Cu<sub>2</sub>Sb(101)</b>	-0.50	0.34	-0.84	-1.84

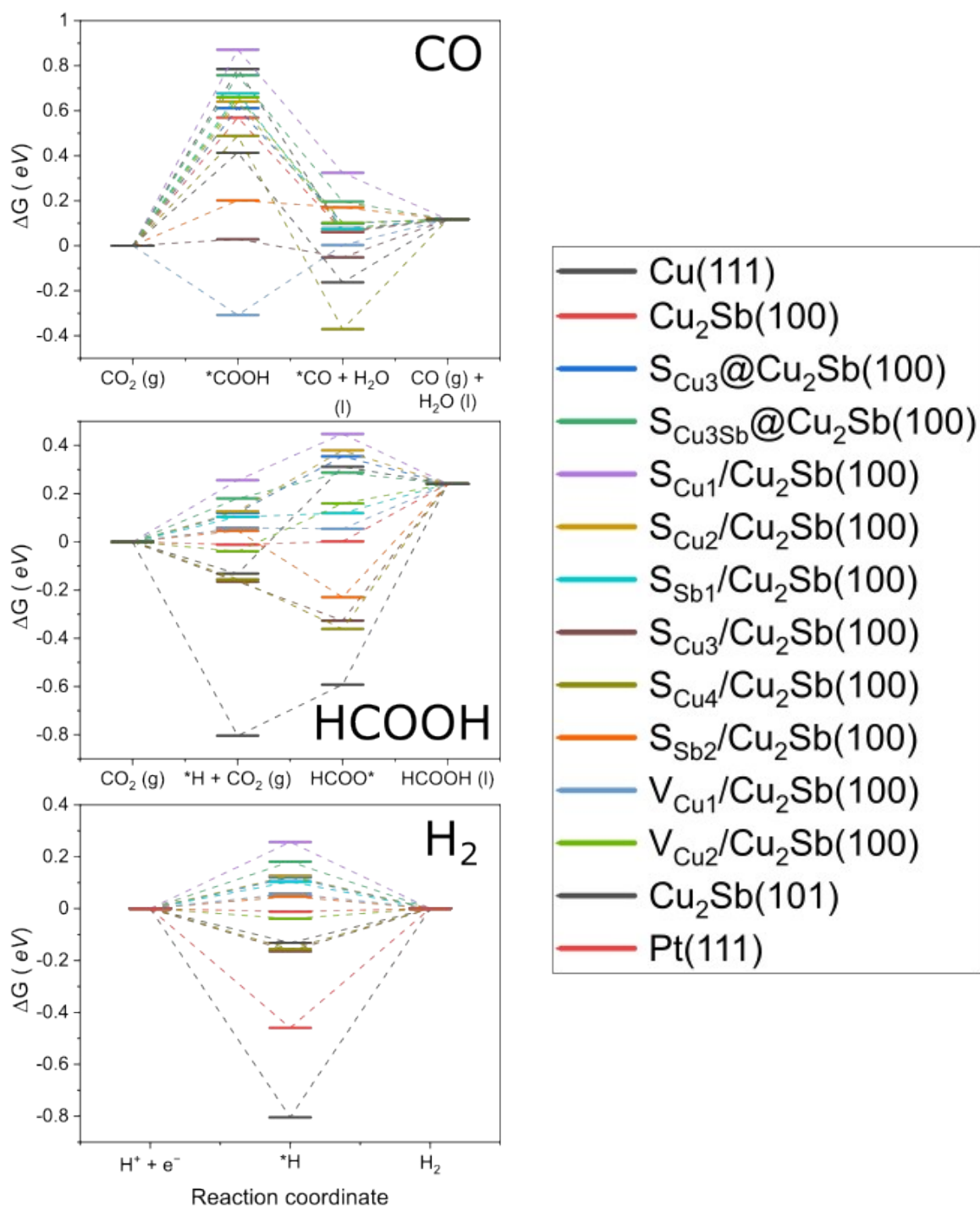


**Figure S21:** Free energy diagrams of all three reaction pathways at 0V

**Table S9. Gibbs energy change for each elementary step considered in equations S13 – S15 for the 2e-CO<sub>2</sub>RR CO pathway at 0.0 V.** The Gibbs energy changes at any applied potential can be calculated, in principle, using the computational hydrogen electrode approach.

Surface Structure	$\Delta_{C1}G / \text{eV}$	$\Delta_{C2}G / \text{eV}$	$\Delta_{C3}G / \text{eV}$
-------------------	----------------------------	----------------------------	----------------------------

<b>Cu(111)</b>	0.79	-0.73	0.06
<b>Cu<sub>2</sub>Sb(100)</b>	0.57	-0.50	0.05
<b>S<sub>Cu3</sub>@Cu<sub>2</sub>Sb(100)</b>	0.61	-0.51	0.02
<b>S<sub>Cu3Sb</sub>@Cu<sub>2</sub>Sb(100)</b>	0.76	-0.56	-0.08
<b>S<sub>Cu1</sub>/Cu<sub>2</sub>Sb(100)</b>	0.87	-0.55	-0.21
<b>S<sub>Cu2</sub>/Cu<sub>2</sub>Sb(100)</b>	0.64	-0.56	0.04
<b>S<sub>Sb1</sub>/Cu<sub>2</sub>Sb(100)</b>	0.68	-0.60	0.04
<b>S<sub>Cu3</sub>/Cu<sub>2</sub>Sb(100)</b>	0.03	-0.08	0.17
<b>S<sub>Cu4</sub>/Cu<sub>2</sub>Sb(100)</b>	0.49	-0.86	0.49
<b>S<sub>Sb2</sub>/Cu<sub>2</sub>Sb(100)</b>	0.20	-0.03	-0.05
<b>V<sub>Cu1</sub>/Cu<sub>2</sub>Sb(100)</b>	-0.31	0.31	0.11
<b>V<sub>Cu2</sub>/Cu<sub>2</sub>Sb(100)</b>	0.66	-0.56	0.02
<b>Cu<sub>2</sub>Sb(101)</b>	0.41	-0.58	0.28

**Table S10. Gibbs energy change for each elementary step considered in equations S16 – S18 for the 2e-CO<sub>2</sub>RR formate pathway 0.0 V. The Gibbs energy changes at any applied potential can be calculated, in principle, using the computational hydrogen electrode approach.**

Surface Structure	$\Delta_{F1}G / \text{eV}$	$\Delta_{F2}G / \text{eV}$	$\Delta_{F3}G / \text{eV}$
<b>Cu(111)</b>	-0.13	0.44	0.07
<b>Cu<sub>2</sub>Sb(100)</b>	-0.01	0.01	0.24
<b>S<sub>Cu3</sub>@Cu<sub>2</sub>Sb(100)</b>	0.12	0.23	-0.11
<b>S<sub>Cu3Sb</sub>@Cu<sub>2</sub>Sb(100)</b>	0.18	0.11	-0.05
<b>S<sub>Cu1</sub>/Cu<sub>2</sub>Sb(100)</b>	0.26	0.19	-0.21
<b>S<sub>Cu2</sub>/Cu<sub>2</sub>Sb(100)</b>	0.13	0.25	-0.14
<b>S<sub>Sb1</sub>/Cu<sub>2</sub>Sb(100)</b>	0.10	0.02	0.12
<b>S<sub>Cu3</sub>/Cu<sub>2</sub>Sb(100)</b>	-0.16	-0.16	0.57
<b>S<sub>Cu4</sub>/Cu<sub>2</sub>Sb(100)</b>	-0.16	-0.21	0.60
<b>S<sub>Sb2</sub>/Cu<sub>2</sub>Sb(100)</b>	0.05	-0.28	0.47
<b>V<sub>Cu1</sub>/Cu<sub>2</sub>Sb(100)</b>	0.06	0.00	0.19
<b>V<sub>Cu2</sub>/Cu<sub>2</sub>Sb(100)</b>	-0.04	0.20	0.08
<b>Cu<sub>2</sub>Sb(101)</b>	-0.80	0.21	0.83

**Table S11. Gibbs energy change for each elementary step considered in equations S19 – S20 for the HER pathway 0.0 V. The Gibbs energy changes at any applied potential can be calculated, in principle, using the computational hydrogen electrode approach.**

Surface Structure	$\Delta_{H1}G / \text{eV}$	$\Delta_{H2}G / \text{eV}$
<b>Cu(111)</b>	-0.13	0.13
<b>Cu<sub>2</sub>Sb(100)</b>	-0.01	0.01
<b>S<sub>Cu3</sub>@Cu<sub>2</sub>Sb(100)</b>	0.12	-0.12
<b>S<sub>Cu3Sb</sub>@Cu<sub>2</sub>Sb(100)</b>	0.18	-0.18
<b>S<sub>Cu1</sub>/Cu<sub>2</sub>Sb(100)</b>	0.26	-0.26
<b>S<sub>Cu2</sub>/Cu<sub>2</sub>Sb(100)</b>	0.13	-0.13
<b>S<sub>Sb1</sub>/Cu<sub>2</sub>Sb(100)</b>	0.10	-0.10
<b>S<sub>Cu3</sub>/Cu<sub>2</sub>Sb(100)</b>	-0.16	0.16
<b>S<sub>Cu4</sub>/Cu<sub>2</sub>Sb(100)</b>	-0.16	0.16
<b>S<sub>Sb2</sub>/Cu<sub>2</sub>Sb(100)</b>	0.05	-0.05
<b>V<sub>Cu1</sub>/Cu<sub>2</sub>Sb(100)</b>	0.06	-0.06

<b>V<sub>Cu2/Cu2Sb(100)</sub></b>	-0.04	0.04
<b>Cu<sub>2</sub>Sb(101)</b>	-0.80	0.80
<b>Pt(111)</b>	-0.46	0.46

## References

- [1] Y. Li *et al.*, "Achieving Highly Selective Electrocatalytic CO<sub>2</sub> Reduction by Tuning CuO-Sb<sub>2</sub>O<sub>3</sub> Nanocomposites," *ACS Sustainable Chemistry & Engineering*, vol. 8, no. 12, pp. 4948-4954, 2020/03/30 2020, doi: 10.1021/acssuschemeng.0c00800.
- [2] H. Li *et al.*, "Selective Reduction of CO<sub>2</sub> to CO on an Sb-Modified Cu Electrode: Spontaneous Fabrication and Physical Insight," *ACS Catalysis*, vol. 11, no. 12, pp. 6846-6856, 2021/06/18 2021, doi: 10.1021/acscatal.1c00860.
- [3] S. Mou *et al.*, "Cu<sub>2</sub>Sb decorated Cu nanowire arrays for selective electrocatalytic CO<sub>2</sub> to CO conversion," *Nano Research*, vol. 14, no. 8, pp. 2831-2836, 2021/08/01 2021, doi: 10.1007/s12274-021-3295-1.
- [4] H. Chen *et al.*, "Facile synthesis of an antimony-doped Cu/Cu<sub>2</sub>O catalyst with robust CO production in a broad range of potentials for CO<sub>2</sub> electrochemical reduction," *Journal of Materials Chemistry A*, 10.1039/D1TA06181J vol. 9, no. 40, pp. 23234-23242, 2021, doi: 10.1039/D1TA06181J.
- [5] Z. Zhang *et al.*, "Boosting carbon monoxide production during CO<sub>2</sub> reduction reaction via Cu-Sb<sub>2</sub>O<sub>3</sub> interface cooperation," *Journal of Colloid and Interface Science*, vol. 601, pp. 661-668, 2021/11/01/ 2021, doi: <https://doi.org/10.1016/j.jcis.2021.05.118>.
- [6] J. Zeng *et al.*, "Novel Insights into Sb-Cu Catalysts for Electrochemical Reduction of CO<sub>2</sub>," *Applied Catalysis B: Environmental*, vol. 306, p. 121089, 2022/06/05/ 2022, doi: <https://doi.org/10.1016/j.apcatb.2022.121089>.
- [7] J. Li *et al.*, "Selective CO<sub>2</sub> electrolysis to CO using isolated antimony alloyed copper," *Nature Communications*, vol. 14, no. 1, p. 340, 2023/01/20 2023, doi: 10.1038/s41467-023-35960-z.
- [8] T. Shinagawa, G. O. Larrazábal, A. J. Martín, F. Krumeich, and J. Pérez-Ramírez, "Sulfur-Modified Copper Catalysts for the Electrochemical Reduction of Carbon Dioxide to Formate," *ACS Catalysis*, vol. 8, no. 2, pp. 837-844, 2018/02/02 2018, doi: 10.1021/acscatal.7b03161.
- [9] R. He *et al.*, "Achieving the Widest Range of Syngas Proportions at High Current Density over Cadmium Sulfoselenide Nanorods in CO<sub>2</sub> Electroreduction," *Advanced Materials*, vol. 30, no. 7, p. 1705872, 2018, doi: <https://doi.org/10.1002/adma.201705872>.
- [10] B. J. Skinner, F. D. Luce, and E. Makovicky, "Studies of the Sulfosalts of Copper III; Phases and Phase Relations in the System Cu-Sb-S," *Economic Geology*, vol. 67, no. 7, pp. 924-938, 1972, doi: 10.2113/gsecongeo.67.7.924.
- [11] R. Garcia-Muelas, F. Dattila, T. Shinagawa, A. J. Martin, J. Perez-Ramirez, and N. Lopez, "Origin of the Selective Electroreduction of Carbon Dioxide to Formate by Chalcogen Modified Copper," *J Phys Chem Lett*, vol. 9, no. 24, pp. 7153-7159, Dec 20 2018, doi: 10.1021/acs.jpcclett.8b03212.
- [12] J. K. Nørskov *et al.*, "Origin of the Overpotential for Oxygen Reduction at a Fuel-Cell Cathode," *The Journal of Physical Chemistry B*, vol. 108, no. 46, pp. 17886-17892, 2004/11/01 2004, doi: 10.1021/jp047349j.
- [13] M. T. Tang, H. Peng, P. S. Lamoureux, M. Bajdich, and F. Abild-Pedersen, "From electricity to fuels: Descriptors for C1 selectivity in electrochemical CO<sub>2</sub> reduction," *Applied Catalysis B: Environmental*, vol. 279, 2020, doi: 10.1016/j.apcatb.2020.119384.

- [14] A. A. Peterson, F. Abild-Pedersen, F. Studt, J. Rossmeisl, and J. K. Nørskov, "How copper catalyzes the electroreduction of carbon dioxide into hydrocarbon fuels," *Energy & Environmental Science*, vol. 3, no. 9, 2010, doi: 10.1039/c0ee00071j.
- [15] K. P. Kuhl, T. Hatsukade, E. R. Cave, D. N. Abram, J. Kibsgaard, and T. F. Jaramillo, "Electrocatalytic conversion of carbon dioxide to methane and methanol on transition metal surfaces," *Journal of the American Chemical Society*, vol. 136, no. 40, pp. 14107-13, Oct 8 2014, doi: 10.1021/ja505791r.